The orbit and stellar masses of the archetype colliding-wind binary WR 140

Joshua D. Thomas[1]*, Noel D. Richardson[2]†, Hugues Sana[3], J. J. Eldridge[4],
John D. Monnier[5], Gail H. Schaefer[6], Anthony F. J. Moffat[7], Peredur Williams[8],
Michael F. Corcoran[9,10], Ian R. Stevens[11], Gerd Weigelt[12], Farrah D. Zainol[11],
Narsireddy Anugu[13,14], Jean-Baptiste Le Bouquin[15], Theo ten Brummelaar[6],
Fran Campos[16], Andrew Couperus[1,17], Claire L. Davies[13], Jacob Ennis[5],
Thomas Eversberg[18], Oliver Garde[19], Tyler Gardner[5], Joan Guarro Fló[20],
Stefan Kraus[13], Aaron Labdon[13], Cyprien Lanthermann[3,15], Robin Leadbeater[21],
T. Lester[22], Courtney Maki[1], Brendan McBride[1], J. Ribeiro[23],
Benjamin Setterholm[5], Berthold Stober[24], Mackenna Wood[1], Uwe Zurmuehl[25]

[1]*Department of Physics, Clarkson University, 8 Clarkson Ave, Potsdam, NY 13699, USA*
[2]*Department of Physics and Astronomy, Embry-Riddle Aeronautical University, 3700 Willow Creek Road, Prescott, AZ 86301, USA*
[3]*Institute of Astrophysics, KU Leuven, Celestijnlaan 200D, 3001, Leuven, Belgium*
[4]*Department of Physics, Private Bag 92019, University of Auckland, Auckland 1010, New Zealand*
[5]*Department of Astronomy, University of Michigan, 1085 S. University, Ann Arbor, Michigan 48109, USA*
[6]*The CHARA Array of Georgia State University, Mount Wilson Observatory, Mount Wilson, CA 91023, USA*
[7]*Centre de Recherche en Astrophysique du Québec, Département de physique, Université de Montréal,*
CP 6128, Succ. C.-V., Montréal, QC H3C 3J7
[8]*Institute for Astronomy, University of Edinburgh, Royal Observatory, Blackford Hill,Edinburgh EH9 3HJ*
[9]*CRESST II & X-ray Astrophysics Laboratory, Code 662, NASA Goddard Space Flight Center, Greenbelt, MD 20771, USA*
[10]*Institute for Astrophysics and Computational Sciences, Department of Physics, The Catholic University of America,*
Washington, DC 20064, USA
[11]*School of Physics and Astronomy, University of Birmingham, Edgbaston, Birmingham B15 2TT, UK*
[12]*Max Planck Institute for Radio Astronomy, Auf dem Hügel 69, D-53121 Bonn, Germany*
[13]*University of Exeter, Department of Physics and Astronomy, Exeter, Devon EX4 4QL, UK*
[14]*Steward Observatory, 933 N. Cherry Avenue, University of Arizona, Tucson, AZ 85721, USA*
[15]*Institut de Planétologie et d'Astrophysique de Grenoble, France*
[16]*Observatori Puig d'Agulles, Passatge Bosc 1, 08759, Vallirana, Barcelona, Spain*
[17]*Department of Physics and Astronomy, Georgia State University, 33 Gilmer Street SE Atlanta, GA 30303*
[18]*Schnörringen Telescope Science Institute, Waldbröl, Germany*
[19]*Observatoire de la Tourbiére, 38690 CHABONS, France*
[20]*Balmes 2, 08784 Piera, Barcelona, Spain*
[21]*The Birches Torpenhow, Wigton, Cumbria CA7 1JF, UK*
[22]*1178 Mill Ridge Road, Arnprior, ON, K7S3G8, Canada*
[23]*Observatório do Centro de Informação Geoespacial do Exército - Lisboa, Portugal*
[24]*VdS Section Spectroscopy, Germany; Teide Pro-Am Collaboration*
[25]*D-31180 Giesen, Lower Saxony, Germany*

ABSTRACT

We present updated orbital elements for the Wolf-Rayet (WR) binary WR 140 (HD 193793; WC7pd + O5.5fc). The new orbital elements were derived using previously published measurements along with 163 new radial velocity measurements across the 2016 periastron passage of WR 140. Additionally, four new measurements of the orbital astrometry were collected with the CHARA Array. With these measurements, we derive stellar masses of $M_{\rm WR} = 13.01 \pm 0.20 M_\odot$ (1.5% precision) and $M_{\rm O} = 35.01 \pm 0.30 M_\odot$ (0.8% precision), making this the most precise measurement of a WR star's mass to date. We also include a discussion of the evolutionary history of this system from the Binary Population and Spectral Synthesis (BPASS) model grid to show that this WR star likely formed primarily through mass loss in the stellar winds, with only a moderate amount of mass lost or transferred through binary interactions.

Key words: binaries: general – stars: fundamental parameters – stars: Wolf-Rayet – stars: winds; outflows

1   INTRODUCTION

Mass is the most fundamental property of a star, as it constrains most properties of its evolution. Accurate stellar mass determinations are therefore critical to test stellar evolutionary models and to measure the effects of binary interactions. So far, only two Wolf-Rayet (WR) stars have established visual and double-lined spectroscopic orbits, the hallmark of mass measurements. They are γ^2 Velorum (WC8+O7.5III-V) (North et al. 2007; Lamberts et al. 2017; Richardson et al. 2017) and WR 140 (Fahed et al. 2011; Monnier et al. 2011).

γ^2 Vel contains the closest WR star to us at 336 pc (Lamberts et al. 2017), allowing interferometry to resolve the close 78-d orbit. The only other WR system with a reported visual orbit is WR 140 (Monnier et al. 2011), a long-period highly eccentric system and a benchmark for massive colliding-wind systems, and the subject of this paper. Some progress has been made in increasing this sample by Richardson et al. (2016), who resolved the long-period systems WR 137 and WR 138 with the CHARA Array.

WR 140 is a very intriguing object; with a long period (P=7.928 years) and a high eccentricity ($e = 0.8996$), the system has some resemblance to the enigmatic massive binary η Carinae. It has a double-lined spectroscopic and visual orbit, meaning that we possess exceptional constraints on the system's geometry at any epoch.

WR 140 was one of the first WC stars found to exhibit infrared variability attributed to dust formation (Williams et al. 1978). Its radio, and X-ray emissions, along with the dusty outbursts in the infrared, were originally proposed to be modulated by its binary orbit by Williams et al. (1990). Williams et al. (2009) showed that dust production was indeed modulated by the elliptical orbit. Recently, Lau et al. (submitted) showed that WC binaries with longer orbital periods produced larger dust grains than shorter period systems. Therefore, the accurate determination of all related properties of these binaries can help test this trend, and provide critical constraints on mechanisms that produce dust in these systems.

The orbital properties and apparent brightness of WR 140 make it an important system for the study of binary evolution. As one of the few Wolf-Rayet stars with an exceptionally well-determined orbit, it serves as an important astrophysical laboratory for dust production (e.g., Williams et al. 2009) and colliding-wind shock physics (e.g., Sugawara et al. 2015). In this paper we present refined orbital parameters based on new interferometric and spectroscopic measurements focused on the December 2016 periastron passage. Section 2 presents the observations. We present our new orbital elements and masses in Section 3, and then discuss the evolutionary history of WR 140 in Section 4. We summarize our findings in Section 5.

2   OBSERVATIONS

2.1   Spectroscopic Observations

During the 2016 periastron passage of WR 140, we initiated a global spectroscopic campaign on the system similar to that described by Fahed et al. (2011). In total, we collected 163 spectra over 323 days when the velocities were expected to
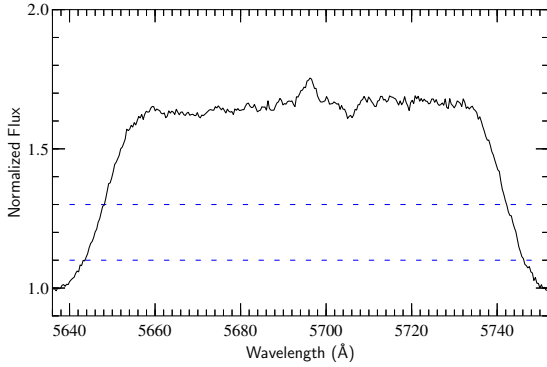
Figure 1. An example C III line profile used for determining the radial velocity of the WR component of the system. This particular spectrum was collected on HJD 2457644.6. The blue dashed lines correspond to the upper and lower bounds of the selection to measure the line center via bisection. These bounds were chosen to minimize contamination from the colliding-wind component of the profile. The small central peak is a C III component from the O-star, and the small absorption near 5705Å is a diffuse interstellar band.

be varying most rapidly. Our measurements are provided in the appendix of this paper in Table A1. The spectra all covered the C III λ5696Å emission-line (broad and narrow components emitted in the WR- and O-star winds, respectively, and from the variable CW region) and the He I λ5876Å line (with emission and P Cygni absorption components from the WR wind, a variable excess emission from the colliding-wind shock-cone, and an absorption component from the O-star's photosphere).

2.1.1 *Radial Velocity Measurements*

The properties of the spectra, and a journal of the observations, are shown in Table 1, and most spectra have a signal-to-noise ratio greater than 100 per resolution element in the continuum. With spectra from so many different sources, we had to ensure that the wavelength calibration was reliable among the various observatories. We therefore checked the alignment of the interstellar Na D absorption lines, and then linearly shifted the spectra by no more than ± 1.3Å to align these lines. With two absorption lines, we were also able to ensure that the spectral dispersion was reliable for the data during this process. An example spectrum of the C III λ5696Å line is shown in Fig. 1.

The velocities of the WR star, shown in the left panel of Fig. 2, were found by bisecting the C III 5696Å emission plateau to find the centroid of the feature. We chose this line due to its relative isolation from other emission features. For example, the C IV $\lambda\lambda$5802, 5812Ådoublet may have been a better choice, but is heavily blended with the He I λ5876Å emission from the WR wind. The spectra were normalized with a linear function so that the low points on either side of the C III feature had a flux of unity. A range of normalized flux values between 1.1, and 1.3 were used to bisect the emission profile as shown in Fig. 1, with the number of flux values used dependent on the resolution of the spectrum. The velocity was then calculated for the average bisector. The displayed error bars are the standard deviation in the

bisection velocity. Our velocity measurements are consistent with predictions from the historical data (e.g., Fahed et al. 2011). A few measurements made just post HJD 2457800 do seem higher than expected for a Keplerian orbit and were weighted less in the fit shown in Section 3. Close examination of the spectra reveals that the colliding-wind excess is likely affecting the red shoulder of the C III emission profile and skews the bisector toward higher redshift in our measurements just after HJD 2457800. The variation in the location of the red shoulder corresponds to skew in the bisector of approximately 30 km s^{-1}, which is roughly the difference between the outliers and the model fit. We did not attempt to correct this, as the number of points affected was small, and this phase of the binary orbit has minimal changes in the radial velocity.

The O-star velocities in the right panel of Fig. 2 were measured by fitting a Voigt profile to the He I λ5875.621Å helium absorption line, which never interferes with any P Cygni absorption from the WR star due to the high WR wind speed. When phase-folded, our O-star velocities are consistent with Fahed et al. (2011). The displayed error bars for the O-star velocity are the uncertainty in the centroid of a Gaussian, for which we used the FWHM from our Voigt profile in equation 15 of Garnir et al. (1987). Again the just post HJD 2457800 data are slightly affected by the changing colliding-wind excess emission. However, as with the WR star velocities, this does not provide a large source of error as the binary orbit has minimal changes in radial velocity at these particular orbital phases.

2.2 Interferometry with the CHARA Array

We have obtained four new epochs of CHARA Array interferometry to measure the precise astrometry of the component stars, following the work of Monnier et al. (2011). The first observation was obtained on 2011 June 17 with the CLIMB beam combiner (Ten Brummelaar et al. 2013). This observation consisted of five observations with the E1, W1, and W2 telescopes. Observations were calibrated with the same calibration stars as Monnier et al. (2011), with the observations of the calibration stars happening before and after each individual scan. These bracketed observations were made in the K'–band and reduced with a pipeline written by John D. Monnier, and were then combined into one measurement to improve the astrometric accuracy.

Another observation was obtained with the MIRC combiner (Monnier et al. 2012b) on UT 2011 September 16. The MIRC combiner uses all six telescopes of the CHARA Array, with eight spectral channels across the H–band. The data were reduced using the MIRC data reduction pipeline (Monnier et al. 2007) using a coherent integration time of 17 ms. We applied a wavelength correction factor of 1.004 to the data based on the analysis by Monnier et al. (2012a). Two additional observations were obtained with the upgraded MIRC-X combiner (Kraus et al. 2018; Anugu et al. 2018) on UT 2018 October 26 and 2019 July 1. The observations were recorded in the PRISM50 mode which provides a spectral resolution of $R = 50$. The data were reduced using the MIRC-X data reduction pipeline, version 1.2.0[1] to produce

---

[1] https://gitlab.chara.gsu.edu/lebouquj/mircx_pipeline.git.

Table 1. List of contributed spectra, in order of number of spectra. The wavelength coverage and range of observation data for each primary observer are noted, as well as the approximate resolving power of their spectra.

Observer	N_{spectra}	λ_{start} (Å)	λ_{end} (Å)	$\text{HJD}_{\text{first}}$ -2450000.5	HJD_{end} -2450000.5	Resolving Power
Guarro	48	3979	7497	7666.89	7944.85	9,000
Thomas	27	5567	6048	7644.12	7918.07	5,000
Leadbeater	17	5623	5968	7615.9	7788.73	5,000
Ribeiro	16	5528	6099	7709.81	7762.76	6,000
Garde	10	4185	7314	7624.91	7759.69	11,000
Berardi	12	5522	6002	7715.73	7778.71	5,000
Campos	12	5463	6212	7675.86	7764.73	5,000
Zurmuehl	11	5620	6469	7684.74	7752.7	4,000
Lester	9	5143	6276	7697.01	7769.94	7,000
Stober	1	4276	7111	7616.82	–	8,000
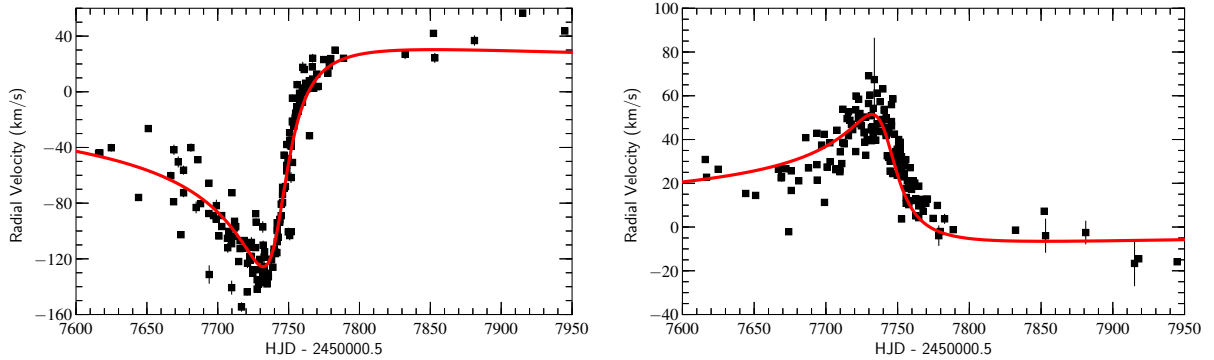
Figure 2. The left panel contains the measured radial velocities from the 2016 periastron passage for the WR star. Error bars shown here represent the standard deviation in the averaged bisector used to determine each velocity. The right panel shows the measured radial velocities for the O-star companion. The error bars represent the uncertainty in the centroid of the line used to calculate the velocity. The error bars in both panels are in most cases smaller than the size of the square representing the data. The red fit curves plotted here corresponds to the orbital elements reported in this paper as "Adopted Fit".

calibrated visibilities and closure phases. During the reduction, we applied the bias correction included in the pipeline and set the number of coherent coadds to 5. A list of the calibrators and their angular diameters (θ_{UD}) adopted from the JMMC catalog (Bourges et al. 2017) are listed in Table 2.

We analyzed the calibrated interferometric data using the same approach as Richardson et al. (2016). More specifically, we performed an adaptive grid search to find the best fit binary position and flux ratio using software[2] developed by Schaefer et al. (2016). During the binary fit, we fixed the uniform disk diameters of the components to sizes of 0.05 mas for the WR star and 0.07 mas for the O-star as determined by Monnier et al. (2011). We added a contribution from excess, over-resolved flux to the binary fit that varied during each epoch. The uncertainties in the binary fit were derived by adding in quadrature errors computed from three sources: the formal covariance matrix from the binary fit, the variation in parameters when changing the coherent integration time used to reduce the data (17 ms and 75 ms for MIRC; 5 and 10 coherent coadds for MIRC-X), and the variation in parameters when changing the wavelength scale

by 0.25% (this was the wavelength precision computed for MIRC, and we applied the same value to MIRC-X; Monnier et al. 2012a). In scaling the uncertainties in the position, we added the three values in quadrature for the major axis of the error ellipse (σ_{major}) and scaled the minor axis (σ_{minor}) to keep the axis ratio and position angle fixed according to the values derived from the covariance matrix. The results of the astrometric measurements are given in Table 3, with significant figures dependent on the individual measurements. In addition to the previously discussed parameters, we include the position angle of the error ellipse (σ_{PA}) in Table 3.

3   THE ORBITAL ELEMENTS

Recently, orbital fits for massive stars with both high-quality spectroscopic and interferometric measurements have become more routine. We applied the same method as discussed in Sana et al. (2013) to iterate on the previous astrometric and spectroscopic orbit of Monnier et al. (2011). With the orbital solution from Monnier et al. (2011) as the starting point, the orbital models were simultaneously adjusted to fit radial velocities (from this work and Fahed et al. 2011), and the interferometric measurements from this work, and from Monnier et al. (2011). The models are adjusted to

---

[2] This software is available at http://chara.gsu.edu/analysis-software/modeling-software.

Table 2. Calibrator stars observed during the MIRC and MIRC-X observations at the CHARA Array.

Star	$\theta_{\rm UD}$ (mas)	Date Observed
HD 178538	0.2487 ± 0.0062	2019Jul01
HD 191703	0.2185 ± 0.0055	2019Jul01
HD 197176	0.2415 ± 0.0058	2019Jul01
HD 201614	0.3174 ± 0.0074	2019Jul01
HD 204050	0.4217 ± 0.0095	2018Oct26
HD 228852	0.5441 ± 0.0127	2018Oct26
HD 182564	0.3949 ± 0.0253	2011Sep16
HD 195556	0.2118 ± 0.0080	2011Sep16
HD 210839	0.4200 ± 0.0200	2011Sep16
HD 214734	0.3149 ± 0.0286	2011Sep16

Table 3. Interferometric measurements with the CHARA Array.

UT Date	HJD -2450000.5	Instrument	Bandpass	Separation (mas)	Position Angle (°)	$\sigma_{\rm major}$ (mas)	$\sigma_{\rm minor}$ (mas)	$\sigma_{\rm PA}$ (°)	$f_{\rm WR}/f_{\rm O}$	Excess Flux (%)
2011Jun17	5729.411	CLIMB	K'	13.02	153.00	0.22	0.06	162		
2011Sep16	5820.270	MIRC	H	12.969	151.749	0.033	0.025	111.65	1.5635 ± 0.4416	5.98 ± 1.91
2018Oct26	8417.139	MIRC-X	H	11.932	155.969	0.030	0.021	141.12	1.1298 ± 0.0044	11.78 ± 0.12
2019Jul01	8665.351	MIRC-X	H	13.018	152.456	0.033	0.015	173.71	1.1003 ± 0.0063	1.26 ± 0.23

minimize the χ^2 statistic. We adopted a minimum 5 km s^{-1} error on the radial velocities so that the radial velocity and astrometric data have the same weight in the final χ^2. When we attempted to fit an orbit with a few ($\lesssim 25$) measurements that had an error smaller than 5 km s^{-1}, we found that the solution would have a larger $\chi^2_{\rm red}$ than our adopted orbit due to their disproportionate weighting. The visual orbit is shown in Fig. 3 and the spectroscopic orbit with all data included is shown in the two panels of Fig. 4.

Monnier et al. (2011) derived an orbital parallax for the system, which yielded a distance of 1.67±0.03 kpc. The *Gaia* Data Release 2 parallax (0.58 ± 0.03 mas) corresponds to a distance of 1.72±0.09 kpc. However, using the work of Bailer-Jones et al. (2018), we find that the Bayesian-inferred *Gaia* distance of $1.64^{+0.08}_{-0.07}$ kpc[3] is consistent with that of Monnier et al. (2011). The Bayesian-inferred distance is preferred as it corrects for the nonlinearity of the transformation and uses an expected Galactic distribution of stars, being thoroughly tested against star clusters with known distances. Our derived orbit, shown in Table 4, was fit with both the *Gaia* distance of 1.64 kpc held constant and with the distance as a free parameter. This model with fixed distance we will refer to as our "Adopted Fit" model in Table 4, while the model with the variable distance is referred to as "Distance Variable". We note that the "Adopted Fit" model does not include the uncertainty in the Bayesian-inferred distance, but that these solutions are within one standard deviation of the distance error at this time.

Given the similarity of the solutions and values for the reduced χ^2 statistic, along with the higher errors on the masses for the free-distance solution, we will adopt the fixed distance ($d = 1.64$ kpc) for the following discussion, but

Figure 3. The visual orbit with the O-star positions relative to the WR star. The WR star location is denoted by the blue star. The data from Monnier et al. (2011) are shown with black × and their error ellipses. The four new epochs of O-star positions are shown as solid cyan circles. The error ellipses on the new points are smaller than the symbol used. The inset plot shows the error ellipses on the new CHARA data. The solid red ellipse is the "Adopted Fit" model from this work. The grey dashed ellipse is the best fit model from Monnier et al. (2011) and the two solutions show remarkable agreement.

---

[3] We also note that Rate & Crowther (2020) derived a distance of $1.64^{+0.11}_{-0.09}$ kpc using Bayesian statistics and a prior tailored for WR stars for the astrometry from *Gaia*.

note that the solution could be revised when the *Gaia* astrometric precision is increased in the future, yielding even more precise absolute masses.

Table 4. Orbital parameters calculated using all historical data plus the new data presented in this paper. The "Adopted Fit" data were calculated using a fixed distance from *Gaia*, modified by proper Bayesian treatment. The "Distance Variable" column represents a fit performed where the distance was a free parameter.

Parameter	Adopted Fit	Distance Variable
P (days)	2895.68 ± 0.17	$2895.67^{+0.16}_{-0.18}$
e	$0.89959^{+0.00082}_{-0.00080}$	$0.90003^{+0.00077}_{-0.00091}$
T_0 (MJD)	$60637.23^{+0.27}_{-0.33}$	$60637.30^{+0.30}_{-0.30}$
ω_{WR} (°)	$225.82^{+0.42}_{-0.39}$	$226.02^{+0.48}_{-0.42}$
$q = \frac{M_{\mathrm{WR}}}{M_{\mathrm{O}}}$	$0.3717^{+0.0054}_{-0.0051}$	$0.3700^{+0.0054}_{-0.0050}$
K_{O} (km s^{-1})	$78.02^{+0.38}_{-0.37}$	$77.91^{+0.37}_{-0.40}$
K_{WR} (km s^{-1})	$29.00^{+0.39}_{-0.38}$	$28.82^{+0.40}_{-0.38}$
γ_{O} (km s^{-1})	$1.17^{+0.39}_{-0.44}$	$0.92^{+0.42}_{-0.43}$
γ_{WR} (km s^{-1})	$4.29^{+0.32}_{-0.32}$	$4.44^{+0.33}_{-0.33}$
i (°)	$120.58^{+0.46}_{-0.45}$	$119.21^{+0.96}_{-1.04}$
Ω (°)	$173.76^{+0.49}_{-0.45}$	$173.11^{+0.65}_{-0.65}$
Distance (kpc)	1.640 (fixed)	$1.598^{+0.022}_{-0.026}$
a (mas)	7.59 ± 0.04	7.75 ± 0.04
a (AU)	$12.44^{+0.07}_{-0.06}$	$12.38^{+0.06}_{-0.07}$
$M_{\mathrm{O}} \sin^3 i$ (M$_\odot$)	$22.34^{+0.33}_{-0.35}$	$22.04^{+0.38}_{-0.37}$
$M_{\mathrm{WR}} \sin^3 i$ (M$_\odot$)	$8.30^{+0.19}_{-0.18}$	$8.15^{+0.20}_{-0.19}$
M_{O} (M$_\odot$)	$35.01^{+0.30}_{-0.32}$	$33.14^{+1.11}_{-1.14}$
M_{WR} (M$_\odot$)	$13.01^{+0.20}_{-0.20}$	$12.26^{+0.46}_{-0.45}$
χ^2	3905	3902
Degrees of Freedom	933	932
χ^2_{red}	4.19	4.19
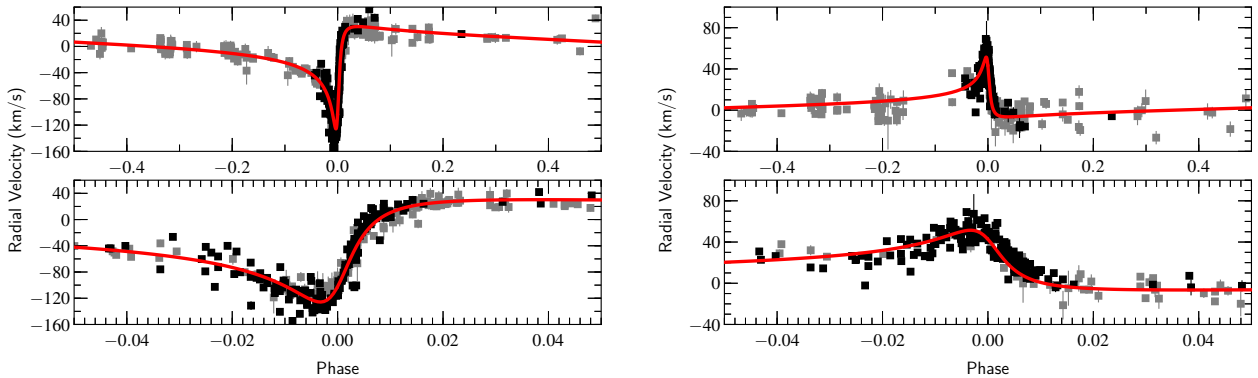
Figure 4. All spectroscopic velocity measurements of WR 140 with our derived "Adopted Fit" (Table 4) in red. The upper left panel shows the all the measurements for the WR component, while the upper right shows the same for the O-star. The lower panels are a factor of ten magnification in the phase near periastron passage. The plotted data include our new results (black) and historical data (grey) from Fahed et al. (2011) and Marchenko et al. (2003).

4 THE EVOLUTIONARY HISTORY OF WR 140

We have attempted to understand the evolutionary history and future of WR 140 by comparing its observational parameters to binary evolution models from the Binary Population And Spectral Synthesis (BPASS) code, v2.2.1 models, as described in detail in Eldridge et al. (2017) and Stanway & Eldridge (2018). Our fitting method is based on that in Eldridge (2009) and Eldridge & Relaño (2011). We use the *UBVJHK* magnitudes taken from SIMBAD where the source is Ducati (2002) and Cutri et al. (2003). We note that the 2MASS magnitudes used here were measured in 1998, and thus were not contaminated by dust created in the 1993 IR maximum. To estimate the extinction, we take the *V*-band magnitude from the model for each time-step and compare it to the observed magnitude. If the model *V*-band magnitude is higher than the observed magnitude we use the difference to calculate the value of A_V. If the model magnitude is less than the observed magnitude we assume zero extinction. We then modify the rest of the model time-step magnitudes with this derived extinction before determining how well that model fits. We then also require that, for an acceptable fit, the model must have a primary star that is hydrogen free, have carbon and oxygen mass fractions that are higher than the nitrogen mass fraction and that the masses of the components and their separation match the observed values that we determine here.

The one caveat in our fitting is that the BPASS models

Table 5. Parameters from BPASS. The primary star evolved into the current WR star.

Initial Parameter	Value
$M_{\mathrm{primary,i}}$ $(M_\odot)$	47.0 ± 8.0
$M_{\mathrm{O,i}}$ $(M_\odot)$	35.4 ± 0.6
$\log(P_\mathrm{i}/d)$	2.19 ± 0.43
Z	0.024 ± 0.013

Present Parameter	Value
$A(V)$	2.4 ± 0.2
$\log(\mathrm{Age}/yr)$	6.65 ± 0.06
$\log(L_{\mathrm{primary}}/L_\odot)$	5.45 ± 0.04
$\log(L_{\mathrm{O}}/L_\odot))$	5.55 ± 0.04
$\log(T_{\mathrm{primary,eff}}/K)$	5.05 ± 0.06
$\log(T_{\mathrm{O,eff}}/K)$	4.47 ± 0.03

assume circular orbits; however, as found by Hurley et al. (2002), stars in orbits with the same semi-latus rectum, or same angular momentum, evolve in similar pathways independent of their eccentricity. A similar assumption was made in Eldridge (2009). Therefore we require that the separation of the model orbit currently is $\log(a/R_\odot) = 2.77$, which is the circular orbital separation with the same evolution as the currently eccentric one. We note that a more realistic model would require including the eccentricity, which can result from binary interactions (e.g., Sepinsky et al. 2007a,b, 2009, 2010) but recalculating new models is beyond the current scope of BPASS and this paper. Given this caveat, we find the current and initial parameters of WR 140, as presented in Table 5.

The matching binary systems tend to interact shortly after the end of the main sequence, thus the mass transfer events occur while the primary star still has a radiative envelope. This may explain why the orbit of WR 140 is still eccentric as deep convective envelopes are required for efficient circularization of a binary. We also note that the mass transfer was highly non-conservative with much of the mass lost from the system. This is evident in that the orbit is significantly longer today than the initial orbit of the order of a year. The companion does accrete a few solar masses of material, so it is possible that the companion may have a significant rotational velocity. Additionally, the companion may be hotter than our models predict here due to the increase in stellar mass. However, we note that the average FWHM of the He I $\lambda 5876$Å line was 140 km s^{-1}, which is fairly normal for young stellar clusters (e.g., Huang & Gies 2006). If the O-star rotates in the plane of the orbit, the rotational speed would be $\sim$ 160 km s^{-1}, slightly larger than typical O-stars (e.g. Ramírez-Agudelo et al. 2013, 2015), but significantly less than predicted if significant accretion would have occured (de Mink et al. 2013). This could also be expected if the situation is as described by Shara et al. (2017) and Vanbeveren et al. (2018), where the O-star's spin-up of the companion could have been braked by the brief appearance of a strong global magnetic field generated in the process (Schneider et al. 2019). Indeed, while some WR+O binaries show some degree of spin-up, that degree is observed to be much less than expected initially after accretion.

While this discussion has used the mean values from all the BPASS models considered, we have taken the most likely

fitting binary and the closest model to this and show their evolution in Figure 5. As we describe above the interactions are modest, because the primary loses a significant amount of mass through stellar winds before mass transfer begins. The interaction is either a short common-envelope evolution which only shrinks the orbit slightly, or only a Roche lobe overflow with the orbit widening. In all cases the star would have become a Wolf-Rayet star without a binary interaction thus making the interactions modest since most mass loss was done via stellar winds.

The most confusing thing about WR 140 is the significantly low estimated age of only 4.5 Myrs ($\log(\mathrm{Age}/yr)$ = 6.65). There are relatively few other stars in the volume of space near WR 140 that would be members of a young cluster. It is therefore a good example of how sometimes clusters may form one very massive star rather than a number of lower-mass stars. The location of the stellar whānau[4] is an open question in its history. It is difficult to make this system older, even if we assume that the Wolf-Rayet star could have been the result of evolution in a triple with WR 140 and the result of a binary merger. Indeed, such a scenario would not explain how such a massive O-star like the companion star could exist. Its presence sets a hard upper limit on the age of the system of approximately 5 Myrs.

5 CONCLUSIONS

We have presented an updated set of orbital elements for WR 140, using newly acquired spectroscopic and interferometric data combined with previously published measurements. The fit was constrained and is consistent with distance measurements from both Monnier et al. (2011) and new measurements from *Gaia*. When using the *Gaia* distance as fixed parameter in the orbital fit, we obtain extremely precise masses for the system of M_{WR} = 13.01 $\pm$ $0.20 M_\odot$ (1.5% precision) and M_{O} = $35.01 \pm 0.30 M_\odot$ (0.8% precision). In comparison, the WR component in γ^2 Vel (WC8) has a mass of $9.0 \pm 0.5 M_\odot$ derived from a visual (interferometric) and spectroscopic orbit (Lamberts et al. 2017), which is lower than the WR component of WR 140, but also carries a higher error on the measurement. Future measurements of more WR binaries will be crucial to test stellar models.

We also discussed the possible evolutionary history of the system in comparison to the BPASS models. The results show that the majority of the envelope is lost by stellar winds with binary interactions only removing a modest amount of material. The measurements presented here should allow for more precise comparisons with the stellar evolutionary and wind models for massive (binary) stars in the future. Furthermore, these results will be used as a foundation for interpretation of multiple data sets that have been collected, including the X-ray variability (Corcoran et al., in prep) and wind collisions (Williams et al., in prep). While these orbital elements are well defined, future interferometric observations with MIRCX will allow for exquisite precision in new measurements, along with additional spectroscopic observational campaigns during periastron passages. MIRCX imaging at the times closest to periastron could pinpoint the

[4] The Māori word for extended family.
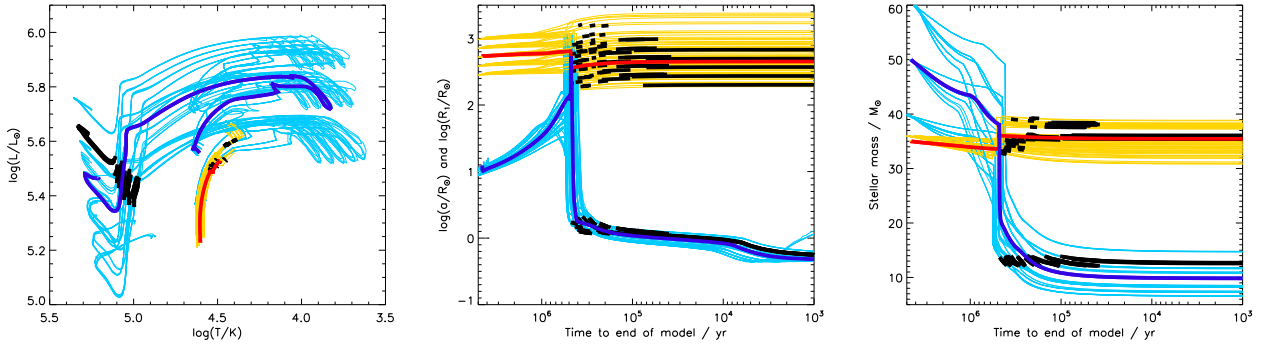
Figure 5. Different aspects of evolution of the WR 140 system are shown in these three panels. In each of the figures the bold lines represent the model with the best matching initial parameters with thinner lined models that are within the 1σ uncertainties in initial mass, initial mass ratio, initial period and initial metallicity. Highlighted in black are the regions of the models where the mass and period of the binary match the "Adopted Fit". In the left panel we show the Hertzsprung-Russell diagram for the past and future evolution, the primary is in blue and the secondary in red. In the central panel we show the primary radius in blue and the orbital separation in red. In the right panel we show the mass of the primary in blue and the mass of the secondary in red.

location of the dust formation in the system, which could be observable in November 2024.

REFERENCES

Anugu N., et al., 2018, in Proc. SPIE. p. 1070124 (arXiv:1807.03809), doi:10.1117/12.2313036

Bailer-Jones C. A. L., Rybizki J., Fouesneau M., Mantelet G., Andrae R., 2018, AJ, 156, 58

Bourges L., Mella G., Lafrasse S., Duvert G., Chelli A., Le Bouquin J. B., Delfosse X., Chesneau O., 2017, VizieR Online Data Catalog, p. II/346

Cutri R. M., et al., 2003, VizieR Online Data Catalog, p. II/246

Ducati J. R., 2002, VizieR Online Data Catalog, II/237,

Eldridge J. J., 2009, MNRAS, 400, L20

Eldridge J. J., Relaño M., 2011, MNRAS, 411, 235

Eldridge J. J., Stanway E. R., Xiao L., McClelland L. A. S., Taylor G., Ng M., Greis S. M. L., Bray J. C., 2017, Publ. Astron. Soc. Australia, 34, e058

Fahed R., et al., 2011, MNRAS, 418, 2

Garnir H.-P., Baudinet-Robinet Y., Dumont P.-D., 1987, Nuclear Instruments and Methods in Physics Research B, 28, 146

Huang W., Gies D. R., 2006, ApJ, 648, 580

Hurley J. R., Tout C. A., Pols O. R., 2002, MNRAS, 329, 897

Kraus S., et al., 2018, in Optical and Infrared Interferometry and Imaging VI. p. 1070123 (arXiv:1807.03794), doi:10.1117/12.2311706

Lamberts A., et al., 2017, MNRAS, 468, 2655

Marchenko S. V., et al., 2003, ApJ, 596, 1295

Monnier J. D., et al., 2007, Science, 317, 342

Monnier J. D., et al., 2011, ApJ, 742, L1

Monnier J. D., et al., 2012a, ApJ, 761, L3

Monnier J. D., Pedretti E., Thureau N., Che X., Zhao M., Baron F., ten Brummelaar T., 2012b, in Optical and Infrared Interferometry III. p. 84450Y, doi:10.1117/12.926433

North J. R., Tuthill P. G., Tango W. J., Davis J., 2007, MNRAS, 377, 415

Ramírez-Agudelo O. H., et al., 2013, A&A, 560, A29

Ramírez-Agudelo O. H., et al., 2015, A&A, 580, A92

Rate G., Crowther P. A., 2020, MNRAS, p. 34

Richardson N. D., et al., 2016, MNRAS, 461, 4115

Richardson N. D., et al., 2017, MNRAS, 471, 2715

Sana H., Le Bouquin J. B., Mahy L., Absil O., De Becker M., Gosset E., 2013, A&A, 553, A131

Schaefer G. H., et al., 2016, AJ, 152, 213

Schneider F. R. N., Ohlmann S. T., Podsiadlowski P., Röpke F. K., Balbus S. A., Pakmor R., Springel V., 2019, Nature, 574, 211

Sepinsky J. F., Willems B., Kalogera V., 2007a, ApJ, 660, 1624

Sepinsky J. F., Willems B., Kalogera V., Rasio F. A., 2007b, ApJ, 667, 1170

Sepinsky J. F., Willems B., Kalogera V., Rasio F. A., 2009, ApJ, 702, 1387

Sepinsky J. F., Willems B., Kalogera V., Rasio F. A., 2010, ApJ, 724, 546

Shara M. M., Crawford S. M., Vanbeveren D., Moffat A. F. J., Zurek D., Crause L., 2017, MNRAS, 464, 2066

Stanway E. R., Eldridge J. J., 2018, MNRAS, 479, 75

Sugawara Y., et al., 2015, PASJ, 67, 121

Ten Brummelaar T. A., et al., 2013, Journal of Astronomical Instrumentation, 2, 1340004

Vanbeveren D., Mennekens N., Shara M. M., Moffat A. F. J., 2018, A&A, 615, A65

Williams P. M., Beattie D. H., Lee T. J., Stewart J. M., Antonopoulou E., 1978, MNRAS, 185, 467

Williams P. M., van der Hucht K. A., Pollock A. M. T., Florkowski D. R., van der Woerd H., Wamsteker W. M., 1990, MNRAS, 243, 662

Williams P. M., et al., 2009, MNRAS, 395, 1749

de Mink S. E., Langer N., Izzard R. G., Sana H., de Koter A., 2013, ApJ, 764, 166

APPENDIX A: RADIAL VELOCITY MEASUREMENTS

This paper has been typeset from a TeX/LaTeX file prepared by the author.

Table A1. Measured radial velocities for the new spectra presented in this paper.

HJD−2450000.5	WR Velocity (km/s)	O Velocity (km/s)	Source
7615.90850	−44.1 ± 0.5	30.9 ± 0.3	Leadbeater
7616.82776	−43.9 ± 2.3	22.8 ± 0.2	Stober
7624.91809	−40.2 ± 2.8	26.4 ± 0.1	Garde
7644.12032	−75.9 ± 2.3	15.3 ± 0.7	Clarkson
7651.01573	−26.4 ± 1.7	14.4 ± 0.9	Clarkson
7666.89338	−60.2 ± 2.8	26.5 ± 0.1	Guarro
7668.83826	−79.0 ± 1.5	22.5 ± 0.1	Guarro
7669.09369	−41.7 ± 3.7	23.0 ± 2.2	Clarkson
7672.14171	−50.4 ± 3.9	26.6 ± 0.3	Clarkson
7674.06423	−102.7 ± 1.6	−2.2 ± 0.3	Clarkson
7675.86058	−56.3 ± 3.2	16.7 ± 0.3	Campos
7675.89578	−72.6 ± 3.2	25.7 ± 0.1	Guarro
7681.06131	−40.1 ± 2.9	21.1 ± 0.9	Clarkson
7684.74616	-83.1 ± 4.2		Zurmuehl
7685.99396	−48.8 ± 2.4	40.9 ± 0.4	Clarkson
7687.88062	−80.3 ± 2.3	27.0 ± 0.1	Guarro
7693.78032	−65.7 ± 1.3	42.9 ± 0.3	Leadbeater
7693.78366	−87.4 ± 1.9	28.5 ± 0.2	Guarro
7693.96228	−131.3 ± 6.6	21.5 ± 0.0	Zurmuehl
7697.01575	−88.9 ± 1.1	37.5 ± 1.5	Lester
7698.83037	−91.4 ± 1.2	42.4 ± 0.2	Guarro
7699.02642	−81.8 ± 4.3	11.3 ± 0.5	Clarkson
7700.83225	−103.6 ± 1.6	27.4 ± 0.2	Guarro
7702.75581	−88.9 ± 1.1	38.5 ± 1.4	Leadbeater
7702.87022	−96.8 ± 1.9	29.9 ± 1.5	Guarro
7706.85286	−105.3 ± 1.7	26.2 ± 0.1	Guarro
7707.06650	−112.0 ± 3.6	26.6 ± 0.1	Clarkson
7707.74176	−100.3 ± 1.5	44.2 ± 1.3	Leadbeater
7709.81017	−140.7 ± 5.0	25.3 ± 0.2	Ribiero
7709.81296	−109.1 ± 1.8	26.3 ± 0.1	Guarro
7710.04092	−72.5 ± 2.4	34.4 ± 1.3	Clarkson
7711.07536	−103.7 ± 1.6	29.0 ± 0.5	Clarkson
7711.82039	−97.8 ± 2.5	38.7 ± 0.5	Zurmuehl
7711.84949	−93.0 ± 2.2	53.8 ± 1.6	Leadbeater
7712.70276	−96.9 ± 0.7	38.0 ± 0.3	Leadbeater
7714.75764	−121.9 ± 1.7	49.5 ± 0.9	Ribiero
7715.71599	−106.9 ± 1.2	52.7 ± 0.8	Leadbeater
7715.73729	−112.7 ± 1.0	41.7 ± 0.2	Berardi
7716.74869	−154.6 ± 3.4	48.8 ± 0.4	Zurmuehl
7717.79801	−112.4 ± 1.6	47.0 ± 1.6	Guarro
7718.71246	−106.8 ± 1.7	44.5 ± 0.2	Garde
7720.73462	−108.8 ± 2.2	53.6 ± 1.6	Zurmuehl
7720.77745	−143.8 ± 2.6	34.5 ± 0.2	Ribiero
7720.99044	−123.2 ± 3.4	59.9 ± 1.2	Clarkson
7722.74233	−118.2 ± 1.9	49.7 ± 0.3	Guarro
7722.77181	−120.9 ± 1.8	51.2 ± 0.7	Berardi
7722.80655	−111.7 ± 2.5	58.4 ± 0.2	Campos
7723.74669	−108.2 ± 3.8	51.9 ± 0.4	Campos
7723.75284	−118.3 ± 1.8	47.2 ± 0.3	Guarro
7724.74938	−127.9 ± 1.6	50.1 ± 0.4	Guarro
7724.75337	−130.2 ± 1.3	46.3 ± 1.7	Campos
7726.68947	−111.9 ± 2.0	43.1 ± 1.6	Garde
7726.78215	−87.6 ± 1.2	43.4 ± 1.1	Zurmuehl
7727.06099	−93.6 ± 2.5	38.8 ± 0.9	Clarkson
7727.76572	−134.9 ± 2.2	32.8 ± 0.4	Ribiero
7727.76960	−141.8 ± 2.5	50.3 ± 0.3	Zurmuehl
7728.75588	−138.3 ± 3.3	40.0 ± 1.3	Ribiero
7729.72349	−120.4 ± 0.9	56.5 ± 0.4	Guarro
7729.79283	−127.8 ± 5.3	69.1 ± 0.3	Campos
7730.73046	−135.4 ± 2.7	60.3 ± 0.5	Guarro

HJD−2450000.5	WR Velocity (km/s)	O Velocity (km/s)	Source
7731.69913	−128.1 ± 1.8	50.9 ± 0.5	Berardi
7731.74248	−130.8 ± 2.3	45.4 ± 1.8	Guarro
7731.75590	−137.1 ± 2.5	39.5 ± 1.5	Ribiero
7731.76974	−97.1 ± 4.1	44.4 ± 0.2	Campos
7732.00337	-110.1 ± 3.2		Clarkson
7732.69730	−118.8 ± 3.9	45.9 ± 1.2	Garde
7732.89655	−125.6 ± 2.9	42.7 ± 0.4	Leadbeater
7733.04298	−114.9 ± 3.0	54.2 ± 0.3	Clarkson
7733.78171	−135.0 ± 3.6	67.4 ± 19.1	Campos
7734.74934	−132.3 ± 1.2	43.9 ± 1.6	Guarro
7734.75611	−138.0 ± 2.0	39.7 ± 0.2	Ribiero
7735.69391	−130.4 ± 2.2	47.2 ± 0.8	Garde
7735.73915	−132.9 ± 3.1	61.2 ± 0.3	Guarro
7737.75114	−120.7 ± 3.9	57.3 ± 1.5	Guarro
7737.99405	−120.2 ± 2.4	43.6 ± 0.8	Clarkson
7738.92489	−126.0 ± 2.4	47.3 ± 0.5	Clarkson
7739.69769	−115.6 ± 1.9	63.1 ± 0.3	Leadbeater
7739.72805	−113.0 ± 1.9	49.2 ± 1.0	Guarro
7740.70156	−116.2 ± 1.9	53.3 ± 0.3	Berardi
7740.72612	−115.2 ± 2.3	53.8 ± 0.4	Guarro
7741.75243	−115.5 ± 3.3	45.4 ± 0.4	Ribiero
7741.93606	−94.0 ± 1.9	49.9 ± 0.4	Lester
7741.95381	−107.7 ± 4.7	41.8 ± 1.5	Clarkson
7741.96782	−99.2 ± 2.5	43.1 ± 0.5	Lester
7741.99769	−99.6 ± 2.2	49.0 ± 0.4	Lester
7742.75752	−104.5 ± 1.4	32.6 ± 1.5	Ribiero
7743.70079	−91.7 ± 1.6	43.1 ± 0.5	Berardi
7743.71815	−91.8 ± 1.1	31.8 ± 0.4	Zurmuehl
7743.75725	−93.6 ± 1.4	43.2 ± 0.3	Guarro
7744.75494	−89.0 ± 1.9	25.6 ± 1.5	Ribiero
7744.76281	−80.6 ± 1.7	30.2 ± 0.2	Guarro
7745.70176	−73.9 ± 1.4	48.2 ± 0.9	Berardi
7745.72762	−79.7 ± 3.0	56.0 ± 1.4	Guarro
7745.74729	−68.6 ± 1.7	46.2 ± 0.6	Campos
7746.74793	−69.2 ± 1.6	58.6 ± 1.1	Guarro
7746.76355	−45.5 ± 2.5	24.4 ± 0.5	Campos
7747.75535	−68.0 ± 4.3	42.5 ± 0.3	Garde
7748.70943	−52.8 ± 1.5	30.1 ± 0.2	Berardi
7748.72376	−56.8 ± 1.3	31.8 ± 0.2	Guarro
7748.75753	−37.9 ± 2.8	34.5 ± 0.2	Ribiero
7749.70118	−49.6 ± 1.5	29.9 ± 1.0	Berardi
7749.72075	−48.1 ± 1.3	35.6 ± 0.3	Guarro
7749.75724	−100.6 ± 3.0	23.7 ± 1.4	Ribiero
7750.69524	−29.4 ± 1.9	37.3 ± 0.3	Leadbeater
7750.71981	−35.1 ± 3.0	40.0 ± 0.3	Guarro
7750.75891	−103.3 ± 3.4	29.7 ± 0.2	Ribiero
7751.70041	−38.4 ± 3.1	35.4 ± 1.3	Garde
7751.70049	−61.6 ± 3.9	27.0 ± 0.4	Zurmuehl
7751.72145	−34.6 ± 1.6	38.7 ± 0.4	Guarro
7751.75795	−100.5 ± 2.1	27.1 ± 0.2	Ribiero
7751.75888	−39.1 ± 3.6	23.7 ± 0.2	Campos
7752.69799	−21.7 ± 3.2	27.4 ± 0.2	Garde
7752.70353	−4.5 ± 2.6	25.6 ± 1.3	Zurmuehl
7752.72110	−21.0 ± 1.8	32.0 ± 0.2	Guarro
7752.73721	−50.8 ± 2.2	3.7 ± 0.9	Campos
7753.72269	−24.8 ± 1.0	22.9 ± 0.2	Guarro
7754.69082	−18.3 ± 2.1	28.2 ± 0.2	Garde
7754.70340	−19.4 ± 1.3	24.6 ± 0.3	Berardi
7754.94876	−15.3 ± 2.5	28.2 ± 0.2	Clarkson
7755.70308	−10.8 ± 3.0	30.8 ± 0.9	Leadbeater
7755.94031	−14.2 ± 1.7	17.6 ± 0.7	Lester
7755.94610	5.1 ± 2.7	10.8 ± 0.8	Clarkson
7755.96300	−13.1 ± 2.0	13.5 ± 0.2	Lester
7756.74935	−14.0 ± 1.7	21.2 ± 0.2	Guarro

HJD−2450000.5	WR Velocity (km/s)	O Velocity (km/s)	Source
7757.70237	−9.8 ± 1.5	10.2 ± 0.7	Berardi
7757.70469	−1.0 ± 2.0	19.6 ± 0.3	Leadbeater
7757.72899	−4.9 ± 2.2	11.3 ± 1.5	Guarro
7758.72732	−5.2 ± 1.9	27.1 ± 1.1	Guarro
7759.69877	−0.2 ± 2.1	20.0 ± 0.2	Garde
7759.72275	2.7 ± 1.1	17.2 ± 0.2	Guarro
7759.76482	−7.3 ± 1.7	18.7 ± 0.3	Ribiero
7759.97778	17.6 ± 4.0	20.1 ± 0.0	Clarkson
7760.73924	2.3 ± 0.9	12.1 ± 0.2	Guarro
7760.95617	16.0 ± 2.3	21.2 ± 0.2	Clarkson
7761.95875	6.2 ± 1.3	20.1 ± 0.5	Lester
7762.74853	1.9 ± 1.9	12.9 ± 0.2	Guarro
7762.76955	2.4 ± 2.9	5.1 ± 0.3	Ribiero
7764.70390	7.8 ± 2.1	9.7 ± 0.4	Berardi
7764.72541	8.0 ± 2.6	18.7 ± 0.1	Guarro
7764.73166	−31.5 ± 2.7	4.3 ± 0.5	Campos
7766.72684	6.2 ± 2.1	10.1 ± 0.2	Guarro
7766.74306	17.9 ± 2.3		Leadbeater
7766.94453	9.2 ± 1.0	12.6 ± 0.2	Lester
7766.96052	24.1 ± 3.1	11.4 ± 0.4	Clarkson
7767.73057	2.6 ± 1.4	7.2 ± 0.2	Guarro
7769.73312	3.7 ± 2.6	10.9 ± 0.1	Guarro
7769.94296	12.7 ± 1.6	12.6 ± 0.2	Lester
7770.75387	3.9 ± 2.4	12.8 ± 0.3	Guarro
7774.71494	23.1 ± 1.5	3.9 ± 0.4	Leadbeater
7777.73525	13.4 ± 1.1	9.9 ± 0.3	Guarro
7778.71117	18.6 ± 1.1	−4.0 ± 4.7	Berardi
7779.72978	23.9 ± 1.4	−2.0 ± 0.3	Leadbeater
7782.73860	30.0 ± 1.2	3.7 ± 2.3	Leadbeater
7788.73838	24.1 ± 1.9	−1.2 ± 0.4	Leadbeater
7832.19508	27.0 ± 3.5	−1.4 ± 0.2	Guarro
7852.19978	42.0 ± 1.6	7.2 ± 0.2	Clarkson
7853.13919	24.4 ± 3.6	−4.0 ± 7.8	Guarro
7881.13262	36.8 ± 3.7	−2.5 ± 5.4	Guarro
7915.14428	56.6 ± 1.5	−16.6 ± 10.4	Clarkson
7918.07741	65.3 ± 2.7	−14.5 ± 0.2	Clarkson
7944.85441	43.7 ± 2.1	−15.9 ± 0.3	Guarro
8421.99263	19.0 ± 1.6	−5.9 ± 0.2	Clarkson